



Cascaded lattice Boltzmann method for thermal flows on standard lattices

Linlin Fei^a, Kai H. Luo^{a,b,*}

^a Center for Combustion Energy, Key Laboratory for Thermal Science and Power Engineering of Ministry of Education, Department of Energy and Power Engineering, Tsinghua University, Beijing, 100084, China

^b Department of Mechanical Engineering, University College London, Torrington Place, London, WC1E 7JE, UK

ARTICLE INFO

Keywords:

Lattice Boltzmann method
Cascaded
Thermal flows
2010 MSC:
00-01
99-00

ABSTRACT

In this paper, a thermal cascaded lattice Boltzmann method (TCLBM) is developed in combination with the double-distribution-function (DDF) approach on the standard D2Q9 lattice. A density distribution function relaxed by the cascaded scheme based on central moments is employed to solve the flow field, and a total energy distribution function relaxed by the BGK scheme is used to solve the temperature field. The two distribution functions are coupled naturally to provide a new TCLBM. In this method, the viscous heat dissipation and compression work are taken into account, the Prandtl number and specific-heat ratio are adjustable, and the external force is considered directly without the Boussinesq assumption. The TCLBM is validated by numerical experiments of the thermal Couette flow, low-Mach number shock tube problem, Rayleigh-Bénard convection, and natural convection in a square cavity with a large temperature difference. The simulation results agree well with the analytical solutions and/or results given by previous researchers.

1. Introduction

The lattice Boltzmann method (LBM), based on the kinetic theory, has achieved remarkable success as an alternative method to conventional computational fluid dynamics (CFD) for thermal flow and heat transfer applications during the past three decades [1–9]. Different from solving the discretized Navier-Stokes (N-S) equations in traditional CFD methods, the LBM solves a discrete kinetic equation at the mesoscopic scale, designed to reproduce the N-S equations in the macroscopic limit. The main advantages for LBM over traditional CFD include [10,11]: convenience to deal with complex boundary, easiness of programming, high parallel efficiency, and natural incorporation of micro and meso-scale physics.

The basic algorithm realization of LBM is collision-streaming or streaming-collision, although other time and space evolution schemes can also be used. To be specific, at each time step the collision is first locally executed and followed by streaming the post-collision distributions to their neighbors, or just exchanging the above procedure [12]. Based on this algorithm, various collision operators can be adopted, such as the single-relaxation-time (SRT) or BGK operator [13], two-relaxation-time (TRT) operator [14,15], multiple-relaxation-time (MRT) operator [16,17], and entropic operator [18–20]. Compared with these extensively used operators, cascaded or central moment operator, first proposed by Geier et al. [21] in 2006, is more recent. The

collision in the cascaded Lattice Boltzmann method (CLBM) is performed by relaxing central moments to their local equilibrium values separately, which is different from MRT LBM where the raw moments are relaxed. As mentioned in Ref. [21], central moments can be expressed as polynomials of raw moments of the same order and below. When a raw moment is relaxed (in MRT), all central moments at the same or higher orders will be changed. This “cross-talk” is a source of instability and can be removed in CLBM. By choosing the relaxation parameters properly, CLBM can be adopted to simulate very high Reynolds number flows using coarse grids without adopting any turbulence models or entropic stability [21]. Recently, Lycett-Brown and Luo [22] extended the CLBM to multiphase flow using the interaction potential method [23] with the EDM force scheme [24]. Compared with the LBGK method, the proposed model provided significant improvement in reducing spurious velocities, and increasing the stability range for the Reynolds number and liquid to gas density ratio. They further extended the model to three dimensions and achieved high Weber number, high Reynolds number and high density ratio simultaneously in binary droplet collision simulations [25,26]. More recently, based on a generalized multiple-relaxation-time (GMRT) framework, we proposed a consistent method to incorporate a force field into CLBM and clarified the relation between CLBM and MRT LBM [27].

Although CLBM has obtained success in high Reynolds number single-phase flows and multiphase flows, its applications are so far

* Corresponding author. Center for Combustion Energy, Key laboratory for Thermal Science and Power Engineering of Ministry of Education, Department of Energy and Power Engineering, Tsinghua University, Beijing, 100084, China.

E-mail address: K.Luo@ucl.ac.uk (K.H. Luo).

<https://doi.org/10.1016/j.ijthermalsci.2018.06.017>

Received 31 March 2017; Received in revised form 11 June 2018; Accepted 12 June 2018

1290-0729/© 2018 The Authors. Published by Elsevier Masson SAS. This is an open access article under the CC BY license (<http://creativecommons.org/licenses/by/4.0/>).

limited to incompressible flows. Recently, we showed that for incompressible thermal flows, CLBM can improve the numerical stability significantly compared with the BGK model [9]. The purpose of the present study is to extend CLBM to Low-Mach compressible thermal flows. Generally, there are three feasible ways to construct thermal LBMs. The first one, multispeed approach [28,29], is a straightforward extension of athermal to thermal LBMs, in which more discrete velocities are adopted to match higher-order moment constraints of the density distribution function for recovering the energy equation. In the second one, a density distribution function is still used to simulate the velocity field, while other methods, such as finite difference or finite volume [30,31], are adopted for the temperature field. The double-distribution-function (DDF) [1,2] approach is the third one, where two different distribution functions are adopted to solve flow and temperature fields, respectively. In DDF-based thermal LBMs, the compression work and heat dissipation can be simply included, and the specific-heat ratio and Prandtl number are adjustable. On the whole, the DDF approach keeps the intrinsic features and simple structures of the standard LBM, and more comparisons and discussions among the three methods can be found in Refs. [2,4,32]. In the history, the first DDF thermal model was proposed by He et al. [1] by using an internal-energy-distribution-function-based DDF approach. Guo et al. [2] then presented another DDF thermal model using a total energy distribution function to solve the energy equation, which is simpler than He and co-workers' model. In Guo and co-authors' model, the local temperature in equilibrium density and energy distribution functions is replaced by the reference temperature, thus it is a decoupling model and is limited to Boussinesq flows. In 2012, Li et al. [4] developed a coupling DDF thermal model which can simulate more general thermal flows, and the model was extended to three-dimensions by Feng et al. [33] recently. Inspired by these works, we construct a thermal cascaded lattice Boltzmann method (TCLBM) in the present work based on the DDF approach. In the TCLBM, a density distribution function is relaxed using the cascaded scheme, a total energy distribution function is relaxed using the SRT scheme, and the external force is considered directly without the Boussinesq assumption.

The rest of the paper is structured as follows: Section 2 briefly introduces the cascaded LBM. Section 3 presents a method to incorporate the force field into cascaded LBM. In Section 4, we extend the athermal CLBM to TCLBM. Numerical experiments are carried out for several benchmark problems to validate the proposed model in Section 5. Finally, conclusions of this work are made in Section 6.

2. Cascaded LBM

In this paper, the D2Q9 lattice [13] is adopted, and the discrete velocities are defined as $\mathbf{e}_0 = (0,0)$, $\mathbf{e}_a = (\cos[(a-1)\pi/2], \sin[(a-1)\pi/2])c$, for $a=1-4$, and $\mathbf{e}_a = (\sqrt{2}\cos[(a-9/2)\pi/2], \sqrt{2}\sin[(a-9/2)\pi/2])c$ for $a=5-8$. In LBM, $c = \delta_x/\delta_t$, here δ_x and δ_t are the lattice spacing and time step, and $c = \delta_x = \delta_t = 1$ is used in this work. For the derivation of CLBM, we follow Lycett-Brown and Luo [22] and begin with the velocity moments of the discrete distribution function (DF) f_a , and then f_a and f_a^{eq} can be formulated as functions of the corresponding moments and equilibrium moments.

The raw moments are defined as

$$\rho M_{mn} = \sum_a f_a e_{ax}^m e_{ay}^n \quad (1)$$

in this notation, the zero-order moment $M_{00} = 1$, and first-order moments $M_{10} = u_x$ and $M_{01} = u_y$ are conserved, corresponding to mass, x and y momentum components, respectively. To get the formulations of f_a , another six independent moments are needed, including 3 second-order moments (M_{11} , M_{02} and M_{20}), two third-order moments (M_{21} , M_{12} , noting that M_{03} and M_{30} are not independent of the first-order ones owing to the lack of symmetry in D2Q9 lattice), and the fourth-order

moment M_{22} . Recombining the second-order moments, the trace of the pressure tensor, the normal stress difference and the off diagonal element of the pressure tensor are given by

$$E = M_{20} + M_{02}, \quad N = M_{20} - M_{02}, \quad \Pi = M_{11}. \quad (2)$$

According to the definition above, we get the raw moment representation of populations:

$$f_0 = \rho [M_{00} - E + M_{22}], \quad (3a)$$

$$f_1 = \frac{1}{2}\rho \left[M_{10} + \frac{1}{2}(E + N) - M_{12} - M_{22} \right], \quad (3b)$$

$$f_2 = \frac{1}{2}\rho \left[M_{01} + \frac{1}{2}(E - N) - M_{21} - M_{22} \right], \quad (3c)$$

$$f_3 = \frac{1}{2}\rho \left[-M_{10} + \frac{1}{2}(E + N) + M_{12} - M_{22} \right], \quad (3d)$$

$$f_4 = \frac{1}{2}\rho \left[-M_{01} + \frac{1}{2}(E - N) + M_{21} - M_{22} \right], \quad (3e)$$

$$f_5 = \frac{1}{4}\rho [\Pi + M_{21} + M_{12} + M_{22}], \quad (3f)$$

$$f_6 = \frac{1}{4}\rho [-\Pi + M_{21} - M_{12} + M_{22}], \quad (3g)$$

$$f_7 = \frac{1}{4}\rho [\Pi - M_{21} - M_{12} + M_{22}], \quad (3h)$$

$$f_8 = \frac{1}{4}\rho [-\Pi - M_{21} + M_{12} + M_{22}]. \quad (3i)$$

It should be noted that other variables can also be expressed using their moments in this form similarly.

Central moments are defined in a reference frame shifted by the local velocity,

$$\rho \tilde{M}_{mn} = \sum_a f_a (e_{ax} - u_x)^m (e_{ay} - u_y)^n. \quad (4)$$

The transformation between the raw moments and central moments can be expressed using the binomial theorem as given by Lycett-Brown and Luo [22]. To construct a CLBM, we follow the assumption adopted in Ref. [34], by setting the discrete equilibrium central moments equal to the corresponding continuous values,

$$\rho \tilde{M}_{mn}^{eq} = \int_{-\infty}^{\infty} \int_{-\infty}^{\infty} f^{eq} (\xi_x - u_x)^m (\xi_y - u_y)^n d\xi_x d\xi_y, \quad (5)$$

where f^{eq} is the local Maxwell-Boltzmann distribution for athermal fluid at temperature T_0 in continuous particle velocity space (ξ_x, ξ_y) ,

$$f^{eq} = \frac{\rho}{2\pi RT_0} \exp\left[-\frac{(\xi - \mathbf{u})^2}{2RT_0}\right], \quad (6)$$

and the lattice sound speed $c_s = \sqrt{RT_0}$ is set to be $1/\sqrt{3}$ in this work. Substituting Eq. (6) into Eq. (5), we can calculate the second order and above central moments, and write them using the combination as done in raw moments:

$$\begin{aligned} \tilde{\Pi}^{eq} &= \tilde{N}^{eq} = \tilde{M}_{21}^{eq} = \tilde{M}_{12}^{eq} = 0, \\ \tilde{E}^{eq} &= 2RT_0, \quad \tilde{M}_{22}^{eq} = (RT_0)^2. \end{aligned} \quad (7)$$

The implementation of CLBM is also composed of collision step and streaming step. For the collision step, central moments are relaxed to their equilibrium values, separately:

$$\tilde{\Pi}^* = w_1 \tilde{\Pi}^{eq} + (1 - w_1) \tilde{\Pi}, \quad (8a)$$

$$\tilde{N}^* = w_1 \tilde{N}^{eq} + (1 - w_1) \tilde{N}, \quad (8b)$$

$$\tilde{E}^* = w_2 \tilde{E}^{eq} + (1 - w_2) \tilde{E}, \quad (8c)$$

$$\widetilde{M}_{21}^* = w_3 \widetilde{M}_{21}^{eq} + (1 - w_3) \widetilde{M}_{21}, \quad (8d)$$

$$\widetilde{M}_{12}^* = w_3 \widetilde{M}_{12}^{eq} + (1 - w_3) \widetilde{M}_{12}, \quad (8e)$$

$$\widetilde{M}_{22}^* = w_4 \widetilde{M}_{22}^{eq} + (1 - w_4) \widetilde{M}_{22}, \quad (8f)$$

where w_1 and w_2 are dependent on the shear and bulk viscosities, respectively ($\nu = RT_0(1/w_1 - 0.5)$, and $\nu_B = RT_0(1/w_2 - 0.5)$), and the parameters for the third- and fourth-central moments (w_3 and w_4) are freely tunable to control the stability. The post-collision raw moments can then be recovered according to the binomial theorem,

$$\Pi^* = \widetilde{\Pi}^* + u_x u_y, \quad (9a)$$

$$N^* = \widetilde{N}^* + u_x^2 - u_y^2, \quad (9b)$$

$$E^* = \widetilde{E}^* + u_x^2 + u_y^2, \quad (9c)$$

$$M_{21}^* = \widetilde{M}_{21}^* + 2u_x \Pi^* + \frac{1}{2} u_y (E^* + N^*) - 2u_x^2 u_y, \quad (9d)$$

$$M_{12}^* = \widetilde{M}_{12}^* + 2u_y \Pi^* + \frac{1}{2} u_x (E^* - N^*) - 2u_y^2 u_x, \quad (9e)$$

$$M_{22}^* = \widetilde{M}_{22}^* + 2u_x M_{12}^* + 2u_y M_{21}^* - \frac{1}{2} \mathbf{u}^2 E^* + \frac{1}{2} (u_x^2 - u_y^2) N^* - 4u_x u_y \Pi^* + 3u_x^2 u_y^2. \quad (9f)$$

Then we get the post-collision distribution using Eq. (3), and the streaming step is as usual,

$$f_a(\mathbf{x} + \mathbf{e}_a \delta_t, t + \delta_t) = f_a^*(\mathbf{x}, t). \quad (10)$$

3. Incorporating forcing terms into cascaded LBM

To include the force effect on the flow field, we define f_a changes due to this force field by a source term S_a . To match the overall accuracy in LBM, one way to add the source term in CLBM is to employ the second-order trapezoidal rule along the characteristic line,

$$f_a(\mathbf{x} + \mathbf{e}_a \delta_t, t + \delta_t) = f_a^*(\mathbf{x}, t) + \frac{\delta_t}{2} [S_{a(\mathbf{x}, t)} + S_{a(\mathbf{x} + \mathbf{e}_a \delta_t, t + \delta_t)}]. \quad (11)$$

To remove the implicitness in Eq. (11), the transformation method in Ref. [34] is adopted,

$$\bar{f}_a(\mathbf{x} + \mathbf{e}_a \delta_t, t + \delta_t) = \bar{f}_a^*(\mathbf{x}, t) + \delta_t S_{a(\mathbf{x}, t)}, \quad \bar{f}_a = f_a - \frac{\delta_t}{2} S_a. \quad (12)$$

He et al. [1] proposed that the presence of the force field $\mathbf{F} = (F_x, F_y)$ changes the continuous distribution function as follows:

$$\Delta f^{\mathbf{F}} = \frac{\mathbf{F}}{\rho} \cdot \frac{(\xi - \mathbf{u})}{RT_0} f^{eq}. \quad (13)$$

We then follow the assumption in Ref. [34] that the discrete central moments of S_a are equal to the continuous central moments of $\Delta f^{\mathbf{F}}$:

$$\begin{aligned} \rho \widetilde{M}_{mn}^s &= \sum_a S_a (e_{ax} - u_x)^m (e_{ay} - u_y)^n \\ &= \int_{-\infty}^{\infty} \int_{-\infty}^{\infty} \Delta f^{\mathbf{F}} (\xi_x - u_x)^m (\xi_y - u_y)^n d\xi_x d\xi_y. \end{aligned} \quad (14)$$

Substituting Eq. (13) into the integral, we get the nonzero central moments of S_a ,

$$\widetilde{M}_{10}^s = a_x, \quad (15a)$$

$$\widetilde{M}_{01}^s = a_y, \quad (15b)$$

$$\widetilde{M}_{21}^s = RT_0 a_y, \quad (15c)$$

$$\widetilde{M}_{12}^s = RT_0 a_x. \quad (15d)$$

where a_x and a_y are horizontal and vertical components of the acceleration. As suggested by Premnath and Banerjee [34], we remove third-order moments in Eq. (15) henceforward for convenience. Using the binomial theorem once again, we yield analytical raw moments of S_a ,

$$M_{00}^s = 0, \quad (16a)$$

$$M_{10}^s = a_x, \quad (16b)$$

$$M_{01}^s = a_y, \quad (16c)$$

$$E^s = 2(a_x u_x + a_y u_y), \quad (16d)$$

$$N^s = 2(a_x u_x - a_y u_y), \quad (16e)$$

$$\Pi^s = a_x u_y + a_y u_x, \quad (16f)$$

$$M_{21}^s = a_y u_x^2 + 2a_x u_x u_y, \quad (16g)$$

$$M_{12}^s = a_x u_y^2 + 2a_y u_x u_y, \quad (16h)$$

$$M_{22}^s = 2a_x u_x u_y^2 + 2a_y u_x u_x^2. \quad (16i)$$

Thus, the analytical expressions of S_a can be written in the same form as Eq. (3).

From the definition in Eq. (12), the conserved raw moments of the transformed discrete distribution \bar{f}_a are $\bar{M}_{00} = 1$, $\bar{M}_{10} = u_x - 0.5\delta_t a_x$, and $\bar{M}_{01} = u_y - 0.5\delta_t a_y$, respectively. The corresponding non-conserved raw and central moments can then be obtained straightforwardly,

$$\bar{M}_{pq} = M_{pq} - \frac{1}{2} M_{pq}^s, \quad \widetilde{\bar{M}}_{pq} = \widetilde{M}_{pq}, \quad (p + q > 2). \quad (17)$$

With Eqs. (7) and (15), the non-conserved equilibrium central moments will remain the same as the ones before transformed, thus the collision step for the central moments will not be affected in Eq. (8). According to the relationship between raw moments mentioned above, the post-collision raw moments are slightly different from Eq. (9),

$$\bar{\Pi} = \widetilde{\bar{\Pi}}^* + u_x u_y - \frac{1}{2} (a_x u_y + a_y u_x), \quad (18a)$$

$$\bar{N}^* = \widetilde{\bar{N}}^* + u_x^2 - u_y^2 - (a_x u_x - a_y u_y), \quad (18b)$$

$$\bar{E}^* = \widetilde{\bar{E}}^* + u_x^2 + u_y^2 - (a_x u_x + a_y u_y), \quad (18c)$$

$$\bar{M}_{21}^* = \widetilde{\bar{M}}_{21}^* + 2u_x \bar{\Pi}^* + \frac{1}{2} u_y (\bar{E}^* + \bar{N}^*) - 2u_x^2 u_y + \frac{1}{2} a_y u_x^2 + a_x u_x u_y, \quad (18d)$$

$$\bar{M}_{12}^* = \widetilde{\bar{M}}_{12}^* + 2u_y \bar{\Pi}^* + \frac{1}{2} u_x (\bar{E}^* - \bar{N}^*) - 2u_y^2 u_x + \frac{1}{2} a_x u_y^2 + a_y u_x u_y, \quad (18e)$$

$$\begin{aligned} \bar{M}_{22}^* &= \widetilde{\bar{M}}_{22}^* + 2u_x \bar{M}_{12}^* + 2u_y \bar{M}_{21}^* - \frac{1}{2} \mathbf{u}^2 \bar{E}^* + \frac{1}{2} (u_x^2 - u_y^2) \bar{N}^* \\ &\quad - 4u_x u_y \bar{\Pi}^* + 3u_x^2 u_y^2 - a_x u_x u_y^2 - a_y u_x u_x^2. \end{aligned} \quad (18f)$$

After substituting Eq. (18) into Eq. (3) together with the conserved ones (\bar{M}_{00} , \bar{M}_{10} and \bar{M}_{01}) to get \bar{f}_a^* , the streaming step is then given as:

$$\bar{f}_a(\mathbf{x} + \mathbf{e}_a \delta_t, t + \delta_t) = \bar{f}_a^*(\mathbf{x}, t) + S_{a(\mathbf{x}, t)}. \quad (19)$$

The hydrodynamic variables are then obtained as:

$$\rho = \sum_a \bar{f}_a, \quad \rho \mathbf{u} = \sum_a \bar{f}_a \mathbf{e}_a + 0.5 \mathbf{F} \delta_t. \quad (20)$$

4. Coupling DDF cascaded LBM for thermal flows

For thermal flows, the temperature T is now a function of space and time, not a constant value T_0 . The equilibrium distribution function f^{eq} is given by

$$f^{eq} = \frac{\rho}{2\pi RT} \exp\left[-\frac{(\xi - \mathbf{u})^2}{2RT}\right], \quad (21)$$

and then the reference temperature T_0 in Eq. (7) should be replaced by local temperature T . Inspired by the total-energy-based DDF models [2,4], we adopt a density distribution function relaxed by the cascaded scheme to solve the flow field, together with a total energy distribution function using the BGK relaxation scheme to simulate the temperature field, and the two fields are coupled through the ideal gas equation of state (EOS, $p = \rho RT$). The discrete total energy distribution function has the kinetic equation [2],

$$\partial_t h_a + \mathbf{e}_a \cdot \nabla h_a = -\frac{1}{\tau_h} (h_a - h_a^{eq}) + \frac{Z_a}{\tau_{hf}} (f_a - f_a^{eq}), \quad Z_a = \mathbf{e}_a \cdot \mathbf{u} - \mathbf{u}^2/2. \quad (22)$$

To recover the compressible N-S equations, discrete raw moments of f_a^{eq} should be consistent with the continuous raw moments of f^{eq} from the zeroth to third-order. As mentioned in Sec. 2, two of the third-order raw moments are not independent due to the lack of symmetry in D2Q9 lattice,

$$\sum_a f_a^{eq} e_{ax}^3 = \sum_a f_a^{eq} e_{ax} = \rho u_x, \quad (23a)$$

$$\sum_a f_a^{eq} e_{ay}^3 = \sum_a f_a^{eq} e_{ay} = \rho u_y. \quad (23b)$$

Combining them with $M_{21}^{eq} = u_y RT + u_x^2 u_y$, and $M_{12}^{eq} = u_x RT + u_y^2 u_x$, we have,

$$\sum_a f_a^{eq} e_{ai} e_{aj} e_{ak} = \rho RT (u_k \delta_{ij} + u_j \delta_{ik} + u_i \delta_{kj}) + \rho u_i u_j u_k + \rho u_i (1 - \theta - u_i^2) \delta_{ijkl}. \quad (24)$$

The last term at the RHS is a deviation from the continuous moments for f^{eq} , where $\theta = T/T_0$, and $\delta_{ijkl} = 1$ when $i = j = k = l$, else $\delta_{ijkl} = 0$. This means that the diagonal elements ($\delta_{ijkl} = 1$) for the third-order velocity moments deviate from the needed relationship. As pointed out by Prasianakis and Karlin [35], the deviation can be removed only by adding a correction term C_a into the evolution equation for standard lattices. According to Li and co-workers' work [4], the raw moments for C_a should satisfy,

$$M_{00}^c = M_{10}^c = M_{01}^c = M_{11}^c = 0, \quad (25a)$$

$$E^c = \frac{1}{\rho} \partial_x [\rho u_x (1 - \theta)] + \frac{1}{\rho} \partial_y [\rho u_y (1 - \theta)] \quad (25b)$$

$$N^c = \frac{1}{\rho} \partial_x [\rho u_x (1 - \theta)] - \frac{1}{\rho} \partial_y [\rho u_y (1 - \theta)]. \quad (25c)$$

The other raw moments can be chosen as:

$$M_{21}^c = \frac{1}{\rho} u_y \partial_x [\rho u_x (1 - \theta)], \quad (25d)$$

$$M_{12}^c = \frac{1}{\rho} u_x \partial_y [\rho u_y (1 - \theta)], \quad (25e)$$

$$M_{22}^c = 0. \quad (25f)$$

In the above, all the third-order velocity terms have been neglected because of the low Mach number limit. Then all the central moments for C_a are zero except:

$$\tilde{E}^c = \frac{1}{\rho} \partial_x [\rho u_x (1 - \theta)] + \frac{1}{\rho} \partial_y [\rho u_y (1 - \theta)], \quad (26a)$$

$$\tilde{N}^c = \frac{1}{\rho} \partial_x [\rho u_x (1 - \theta)] - \frac{1}{\rho} \partial_y [\rho u_y (1 - \theta)]. \quad (26b)$$

In the simulation, the derivative terms can be evaluated using a second-order central difference. Then the analytical expressions of C_a can be written in the same form as Eq. (3).

By using a second-order trapezoidal rule, the evolution equation can be written analogously:

$$\begin{aligned} \bar{f}_a(\mathbf{x} + \mathbf{e}_a \delta_t, t + \delta_t) &= \bar{f}_a^*(\mathbf{x}, t) + S_a(\mathbf{x}, t) \delta_t + C_a(\mathbf{x}, t) \delta_t, \quad \bar{f}_a^* \\ &= f_a - \frac{\delta_t}{2} S_a - \frac{\delta_t}{2} C_a. \end{aligned} \quad (27)$$

Due to the non-zero second-order central moments (\tilde{E}^c and \tilde{N}^c) for C_a , the equilibrium central moments for the transformed distribution \bar{f}_a should be:

$$\tilde{M}^{eq} = \tilde{M}_{21}^{eq} = \tilde{M}_{12}^{eq} = 0, \quad (28a)$$

$$\tilde{N}^{eq} = \frac{1}{2\rho} \partial_y [\rho u_y (1 - \theta)] - \frac{1}{2\rho} \partial_x [\rho u_x (1 - \theta)], \quad (28b)$$

$$\tilde{E}^{eq} = 2RT - \frac{1}{2\rho} \partial_x [\rho u_x (1 - \theta)] - \frac{1}{2\rho} \partial_y [\rho u_y (1 - \theta)], \quad (28c)$$

$$\tilde{M}_{22}^{eq} = (RT)^2. \quad (28d)$$

The cascaded relaxation for central moments is in the same form as Eq. (8), while the dynamic viscosity μ and bulk viscosity μ_B are:

$$\mu = p(1/w_1 - 0.5), \quad \mu_B = p(1/w_2 - 0.5). \quad (29)$$

Because the conserved raw moments for C_a are zero, the calculation for post-collision raw moments is the same as Eq. (18). Then \bar{f}_a^* can be obtained using Eq. (3) once again. After the streaming step Eq. (27), hydrodynamic variables are then obtained using Eq. (20).

To recover the total energy equation, the velocity moments for h_a^{eq} should satisfy:

$$M_{00}^{heq} = E, \quad (30a)$$

$$M_{10}^{heq} = (E + RT)u_x, \quad (30b)$$

$$M_{01}^{heq} = (E + RT)u_y, \quad (30c)$$

$$M_{20}^{heq} = (E + 2RT)u_x^2 + RT(E + RT), \quad (30d)$$

$$M_{02}^{heq} = (E + 2RT)u_y^2 + RT(E + RT), \quad (30e)$$

$$M_{11}^{heq} = (E + 2RT)u_x u_y. \quad (30f)$$

where $E = (bRT + \mathbf{u}^2)/2$ is the total energy, in which the gas has b degrees of freedom. Besides, we can set higher raw moments to be zero, so h_a^{eq} can be given by Eq. (3),

$$h_a^{eq} = \begin{cases} \rho [E - (E + 2RT)\mathbf{u}^2 - 2RT(E + RT)], & a = 0 \\ \frac{1}{2}\rho [(E + RT)\mathbf{e}_a \cdot \mathbf{u} + (E + 2RT)(e_{ax}^2 u_x^2 + e_{ay}^2 u_y^2) + RT(E + RT)], & a = 1, \dots, 4 \\ \frac{1}{4}\rho [(E + 2RT)e_{ax} e_{ay} u_x u_y], & a = 5, \dots, 8 \end{cases} \quad (31)$$

In the same manner, we use a transformed total energy distribution function:

$$\bar{h}_a = h_a - \frac{1}{2} K_a, \quad K_a = \frac{Z_a}{\tau_{hf}} \left(\bar{f}_a - f_a^{eq} + \frac{\delta_t}{2} S_a + \frac{\delta_t}{2} C_a \right). \quad (32)$$

Then the time-discrete form of Eq. (22) is,

$$\begin{aligned} \bar{h}_a(\mathbf{x} + \mathbf{e}_a \delta_t, t + \delta_t) - \bar{h}_a(\mathbf{x}, t) &= -w_h [\bar{h}_a(\mathbf{x}, t) - h_a^{eq}(\mathbf{x}, t)] \\ &\quad + (1 - 0.5w_h) K_a(\mathbf{x}, t), \end{aligned} \quad (33)$$

where the relaxation parameters are related to the thermal conductivity λ Prandtl number Pr and the specific-heat coefficients at constant pressure c_p ($c_p = (b + 2)R/2$) [4],

$$w_h^{-1} = \lambda/(pc_p) + 0.5, \quad \tau_{hf} = (\mu/p + 0.5)/(Pr - 1). \quad (34)$$

The macroscopic temperature is obtained by,

$$T = \frac{2}{bR} \left(\sum_a \bar{h}_a / \rho - \frac{1}{2} \mathbf{u}^2 \right). \tag{35}$$

If the compression work and viscous heat dissipation are negligible, we can adopt an analogous internal energy (temperature) distribution function [4] to solve the temperature field. This concludes the development of a new thermal cascaded lattice Boltzmann method (TCLBM).

5. Numerical experiments

In this section, a series of numerical experiments are conducted to verify the developed model. Unless otherwise specified, $w_2 = w_3 = w_4 = 1.0$ is adopted in simulations.

5.1. Thermal Couette flow

To check the capability of describing viscous heat dissipation by the present TCLBM, two-dimensional thermal Couette flow is simulated. We consider the viscous fluid between two infinite parallel plates, in which the upper one is moving at speed U with temperature T_0 and the lower adiabatic plate is fixed. With the assumption that $Pr = \mu c_p / \lambda$ is constant and $(\mu/\mu_0) = (T/T_0)$, there is an analytical solution [36],

$$\left(1 + Pr \frac{\gamma - 1}{3} Ma^2 \right) \frac{y}{H} = \frac{u_x}{U} + Pr \frac{\gamma - 1}{2} Ma^2 \left[\frac{u_x}{U} - \frac{1}{3} \left(\frac{u_x}{U} \right)^3 \right], \tag{36a}$$

$$\frac{T}{T_0} = 1 + Pr \frac{\gamma - 1}{2} Ma^2 \left[1 - \left(\frac{u_x}{U} \right)^2 \right], \tag{36b}$$

where $\gamma = (b + 2)/b$ is the specific-heat ratio, $Ma = U/\sqrt{\gamma RT_0}$ is the Mach number, and H is the distance between the two plates.

In our simulations, we set $Ma = 0.35$ with different values of Pr and γ : $Pr = 4$ with $\gamma = 5/3$ ($b = 3$) and $3/2$ ($b = 4$); $Pr = 5$ with $\gamma = 5/3$ and $3/2$. A uniform mesh $N_x = N_y = 5 \times 60$ is employed. For the top and bottom walls, the non-equilibrium bounce-back method [37] and non-equilibrium extrapolation method [2,38] are adopted for velocity and temperature boundary conditions, respectively, while the periodic boundary condition is imposed along the x direction. The upper wall temperature and the reference temperature are set to unity, with a reference dynamic viscosity $\mu_0 = 0.35$. The relaxation parameter w_1 is a field variable related to the local dynamic viscosity as given in Eq. (29).

Fig. 1 presents the simulation and analytical results for

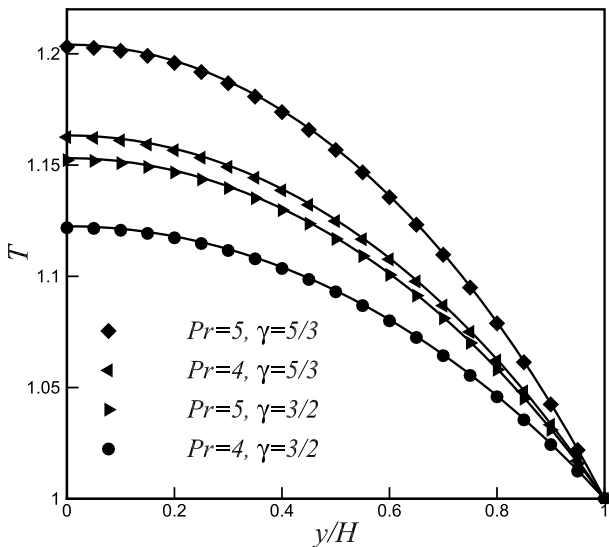


Fig. 1. Comparison between the simulation (symbols) and analytical (solid lines) results for dimensionless temperature profiles at $Ma = 0.35$, with $Pr = 5$ and 4 , $\gamma = 5/3$ and $3/2$, respectively.

Table 1

Comparison of the bottom wall temperatures between numerical and analytical results.

Cases	$Pr = 5$	$Pr = 5$	$Pr = 4$	$Pr = 4$
	$\gamma = 5/3$	$\gamma = 3/2$	$\gamma = 5/3$	$\gamma = 3/2$
T_n	1.2031	1.1524	1.1626	1.1218
T_a	1.2042	1.1531	1.1633	1.1225
E_r	0.54	0.46	0.43	0.57

dimensionless temperature profiles in four cases. It can be observed that numerical results are in excellent agreement with the theoretical ones. To be specific, the temperatures at the bottom wall in numerical (T_n) and analytical (T_a) solutions are compared in Table 1. The relative error is defined as $E_r = |1.0 - (T_n - T_0)/(T_a - T_0)|$. As presented in Table 1, the relative errors are less than 1% in all the cases.

5.2. Low-Mach shock tube problem

To check the present model's ability of simulating Low-Mach number compressible flow, a shock tube problem is studied in this section. The construction of this problem is that a long tube containing the same gas is separated by a barrier in the middle into two parts with different pressures, densities and temperatures. At the moment of removing the barrier, a complex flow is set up. The initial conditions for our simulations are,

$$\begin{cases} (\rho/\rho_0, u_x/u_0, p/p_0) = (1.0, 0.2), & 0 \leq x \leq 0.5 \\ (\rho/\rho_0, u_x/u_0, p/p_0) = (0.5, 0.0, 1), & 0.5 < x \leq 1 \end{cases} \tag{37}$$

where $\rho_0 = 1.0$, $T_0 = 1.0$, $p_0 = \rho_0 RT_0 = 1/3$, $u_0 = \sqrt{\rho_0 RT_0}$ are the reference density, temperature, pressure and velocity, respectively, and L_0 is the length of the tube.

In the simulation, a 1000×5 lattice is used, the periodic boundary condition is imposed along the y direction, while EDFs are used in $x = 0$ and $x = 1000$. The specific heat ratio γ and Prandtl number Pr are set to 1.4 and 0.71, with $w_1 = 1.89$. Simulation results are compared with the analytical ones in Fig. 2. The four plots present dimensionless density, pressure, horizontal velocity, and temperature profiles, respectively, at time $t = 520\delta_t$. It can be observed that numerical results are in good agreement with the theoretical ones.

5.3. Rayleigh-Bénard convection

To check the ability of simulating thermal flow with external force by the present TCLBM, the numerical experiment of the Rayleigh-Bénard convective flow is conducted in this section. The Rayleigh-Bénard instability is one of the classical thermal instability phenomena, in which the fluid is enclosed between two parallel stationary walls, cold at the top and hot at the bottom, and experiences the gravity force. Linear stability theory has proven that convection develops most readily when the wave number is at the critical value 3.117 [40], which is approximately corresponding to length-width ratio 2:1 in the flow domain.

Since the present model is a coupling model, we can implement the force by means of central moments with $a_x = 0$ and $a_y = -g$ (g is the gravity acceleration), without using the Boussinesq assumption. We conduct the experiment in the weakly compressible regime, with a 6% temperature difference of the reference temperature $T_0 = 1.0$. To delete the heat dissipation term, we adopt the internal energy distribution function to simulate temperature field [4,41]. The non-equilibrium extrapolation scheme [2,38] is used to treat the upper and lower wall boundaries for both velocities and temperatures, whereas the periodic boundary scheme is applied along the horizontal direction. The Prandtl number corresponds to air, $Pr = 0.71$. Then the flow is characterized by

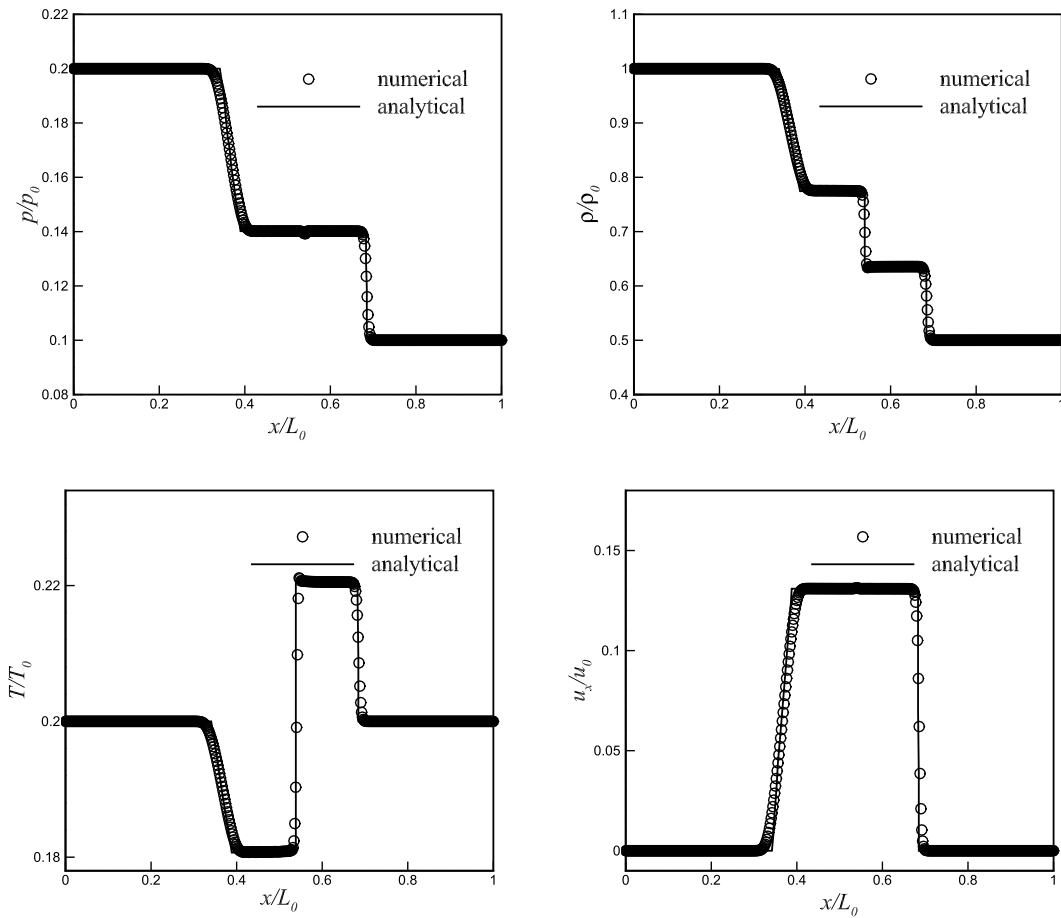


Fig. 2. Comparison between the simulation (symbols) and analytical [39] (solid lines) results for dimensionless density, pressure, horizontal velocity, and temperature profiles at $t = 520\delta$. The symbol spacing is ISkip = 2.

the Rayleigh number Ra ,

$$Ra = \frac{g\beta(T_l - T_h)H^3Pr}{\nu^2}, \tag{38}$$

where T_l and T_h are temperatures of the upper and lower walls ($T_l > T_h$), H is the distance between the walls, and ν is the kinematic viscosity of the fluid. The characteristic velocity $u_c = \sqrt{g\beta(T_h - T_l)H}$ should be set to be an appropriate value, for example 0.08 in our simulation, to keep the flow in the low-Mach number regime. And β is the thermal expansion coefficient, which is the reciprocal of reference temperature for the ideal gas considered here.

For this kind of instability phenomenon, the driven force by the density variations induced by the temperature variations will balance with the viscosity force at the critical Rayleigh number Ra_c , while if the Rayleigh number is increased above the threshold, the driving force will dominate and convection will start. First, we use a $N_x \times N_y = 200 \times 100$ grid to calculate the critical Rayleigh number. We initialize the temperature field with a linear distribution in the y direction and give a small perturbation for density around the reference density $\rho_0 = 1.0$. It is noted that the total kinetic energy will keep increasing/decreasing lineally after the initial unsteady period around the critical Rayleigh number. For that, the total kinetic energy increment Δe every 10000 time steps in the domain is measured,

$$\Delta e = e(t + 10000) - e(t), \quad e(t) = \sum \left[\frac{1}{2} \rho(x, y, t) \mathbf{u}^2(x, y, t) \right]. \tag{39}$$

where Δe is measured by the slope of the total kinetic energy change with time, not at a certain time step. The critical Rayleigh number extrapolated is $Ra_c = 1707.07$ (see Fig. 3), which is in excellent

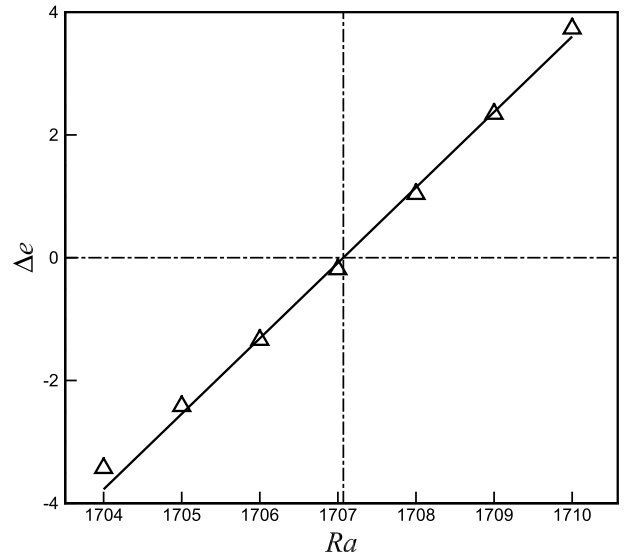


Fig. 3. Total internal energy increment $\Delta e (\times 10^{-10})$ changes with different Rayleigh numbers. Triangles are the numerical results; the solid line is the linear fit for the simulations. The critical Rayleigh number extrapolated is $Ra_c = 1707.07$.

agreement with the analytical value 1707.76.

Flows of different Rayleigh numbers are then simulated, $N_y = 80$ is used if $Ra < 10000$, $N_y = 100$ if $10000 \leq Ra < 50000$ and $N_y = 150$ for $Ra \geq 50000$. The normalized temperature distribution for Rayleigh-

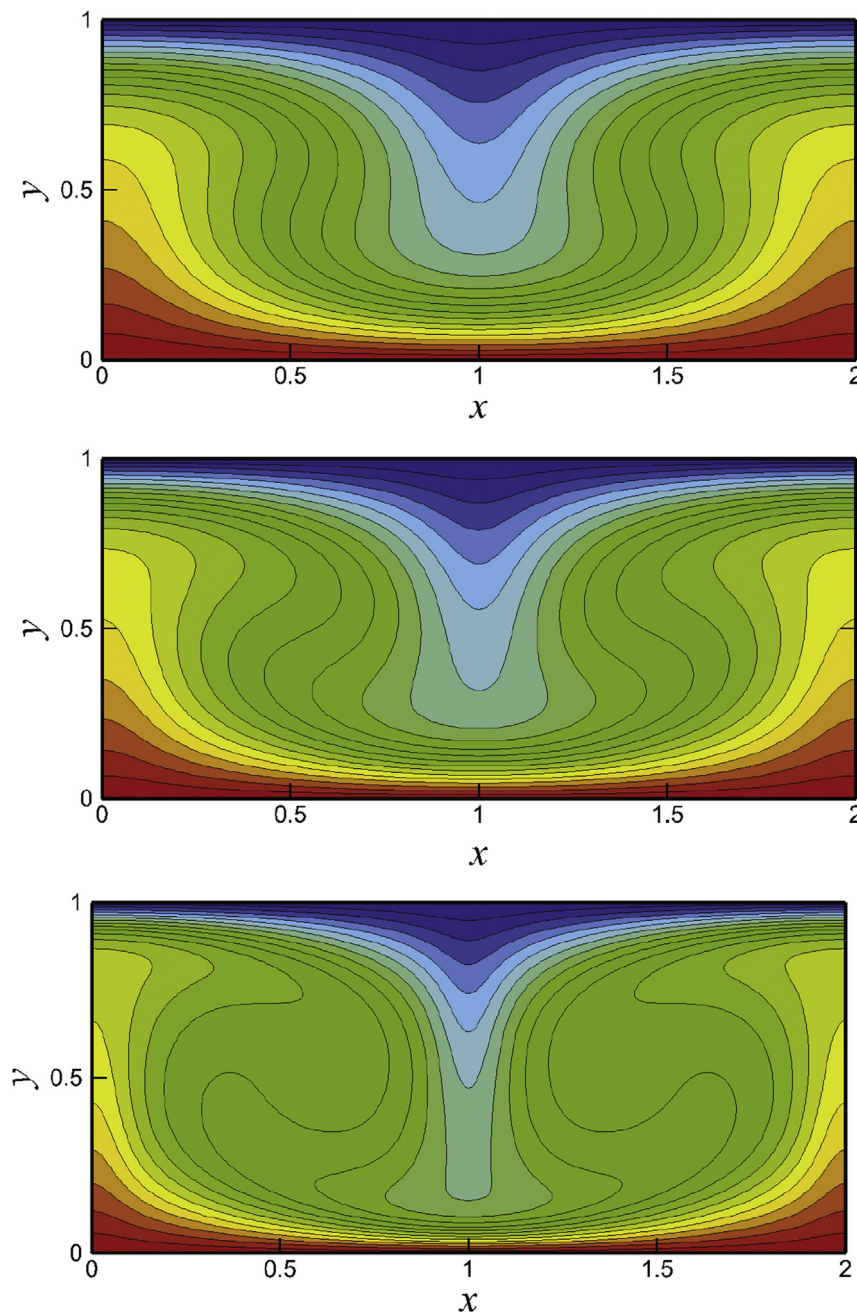


Fig. 4. The normalized temperature $(T - T_0)/\Delta T$ distribution for Rayleigh-Bénard convection flow. From top to bottom: $Ra = 5000, 10000$ and 50000 . A total of 19 equidistant lines are plotted.

Bénard convection at $Ra = 5000, 10000$ and 50000 are shown in Fig. 4. When the Rayleigh number increases, we can see two clear trends in the figures: the mixing of the hot and cold fluids is enhanced, and the temperature gradients near the bottom and top walls are increased, both of which mean the convective heat transfer is enhanced in the domain. To quantify this, the Nusselt number in the system is calculated,

$$Nu = 1 + \frac{\langle u_y T \rangle H}{k \Delta T}, \tag{40}$$

where the square bracket represents the average over the whole system and k is the thermal conductivity of the fluid. The obtained values of Nusselt number Nu_n at various Rayleigh numbers are compared with the reference data in Table 2, and plotted in Fig. 5. The simulation results are in good agreement with those of Ref. [40] in a wide range of

Table 2

Comparison of Nusselt number between the present numerical results and the results in Ref. [40].

Cases	$Ra = 2500$	$Ra = 5000$	$Ra = 10000$	$Ra = 30000$	$Ra = 50000$
Nu_n	1.468	2.106	2.650	3.629	4.181
Ref. [40]	1.475	2.116	2.661	3.662	4.245
$E_R(\%)$	0.47	0.47	0.41	0.90	1.51

Ra as given in Table 2. During the small Rayleigh number range ($Ra < 5000$), convection is suppressed so that the Nusselt number decreases rapidly to 1.0 at $Ra = Ra_c$, where the empirical formula loses efficacy. At very high Rayleigh numbers, the numerical results slightly underestimate the heat transfer, while this trend was also observed in other LBM studies [1,33,35].

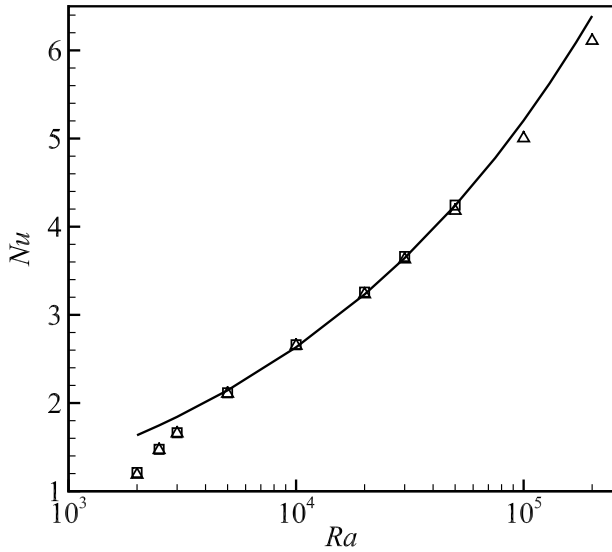


Fig. 5. Nusselt number vs Rayleigh number. Triangles: the present thermal CLBM; squares: reference data from Ref. [40]; and solid line: the empirical formula $Nu = 1.56(Ra/Ra_c)^{0.296}$.

5.4. Natural convection in a square cavity

In this subsection, the present TCLBM is employed to simulate the natural convection in a square cavity. In this case, the large temperature difference condition is considered, in which the left and right walls are

maintained at $T_h = 960$ K and $T_l = 240$ K respectively, and the horizontal sidewalls are adiabatic. The dynamic viscosity is defined by the Sutherland's Law:

$$\frac{\mu}{\mu^*} = \left(\frac{T}{T^*}\right)^{3/2} \frac{T^* + S}{T + S} \tag{41}$$

where $T^* = 273$ K, $S = 110.5$ K. The μ^* is the dynamic viscosity at T^* , which is determined from the reference viscosity μ_r at the reference temperature $T_r = 600$ K. In the simulation. The Prandtl number is taken as 0.71, μ_r is set to be 0.14, 0.1, 0.06, and 0.055 for $Ra = 10^3, 10^4, 10^5,$ and 10^6 , and the grid sizes are $100 \times 100, 150 \times 150, 250 \times 250$ and 650×650 , respectively. The isotherms and streamlines are presented in Figs. 6 and 7. The streamlines are drawn through the numerical integration of the steady compressible stream function ($\partial_x \psi = -\rho u_y, \partial_y \psi = \rho u_x$), where the partial derivative is discretized by the second-order central difference. The asymmetry feature of the convection with a large temperature difference is clearly shown in Figs. 6 and 7: For $Ra = 10^3$ and 10^4 , the center of the primary vortex shifts to the lower right side of the cavity center, and the two small vortices at higher Rayleigh numbers are not similar in size and shape, which agree well with the benchmark solutions given in Ref. [42].

To quantify the results, the average Nusselt number of the left wall and the maximum velocity components (normalized by the reference velocity $V_{ref} = \mu_r / (PrH)$) across the vertical and horizontal mid-planes are computed. The local and averaged Nusselt numbers are defined as $Nu(y) = H\lambda \cdot \partial T_{wall} / [\lambda_r(T_h - T_l)]$ and $Nu = \int_0^H Nu(y) dy / H$ [4,42]. The results predicted by the present TCLBM are compared with the previous benchmark solutions [42] and LB results [4] in Table 3. From the table we can see that the present results are in good agreement with the data

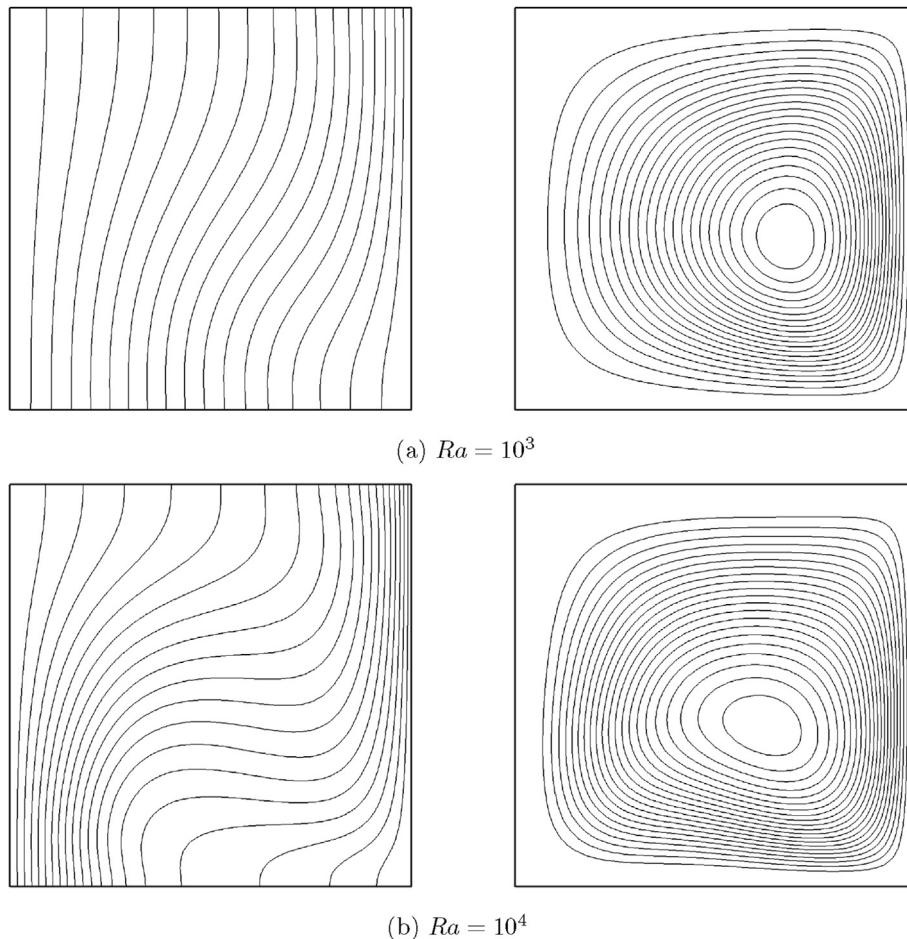


Fig. 6. Isotherms (left) and streamlines (right) of natural convection in a square cavity at $Ra = 10^3$ and $Ra = 10^4$.

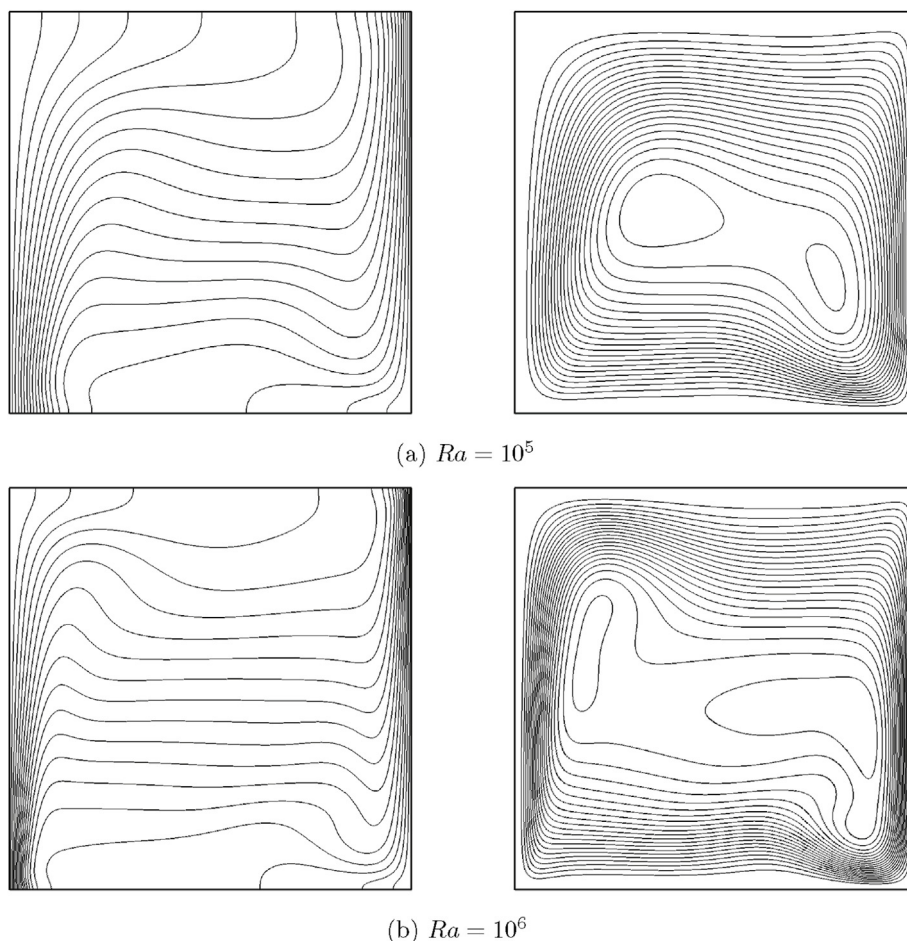


Fig. 7. Isotherms (left) and streamlines (right) of natural convection in a square cavity at $Ra = 10^5$ and $Ra = 10^6$.

Table 3
Comparisons of the present results with the Benchmark [42] and LB [4] solutions.

Ra		Nu	$ u _{\max}$	y_{\max}	$ v _{\max}$	x_{\max}
10^3	Benchmark [42]	1.108	3.702	0.1618	4.324	0.9036
	LB [4]	1.111	3.726	0.1600	4.429	0.9100
	Present	1.106	3.681	0.1624	4.323	0.9063
10^4	Benchmark [42]	2.218	16.777	0.7821	20.327	0.9270
	LB [4]	2.217	16.786	0.7800	20.404	0.9267
	Present	2.224	16.841	0.7813	20.299	0.9312
10^5	Benchmark [42]	4.480	43.692	0.8364	71.084	0.0948
	LB [4]	4.454	43.984	0.8360	71.070	0.0960
	Present	4.512	43.805	0.8344	71.303	0.0938
10^6	Benchmark [42]	8.687	84.703	0.8541	227.414	0.0537
	LB [4]	–	–	–	–	–
	Present	8.691	85.332	0.8551	224.312	0.0540

in previous works.

6. Conclusions

In this paper, we developed a thermal cascaded lattice Boltzmann method (TCLBM) for low-Mach compressible thermal flows on standard lattices. Considering the proven numerical performances of DDF-based thermal LBMs, we constructed the TCLBM in this framework. Firstly, the reference temperature in equilibrium central moments for the density DF was replaced by the local temperature. Secondly, a correction term was introduced similarly by means of central moments to remove the derivation of two diagonal elements for the third-order raw

moments. Then a total energy EDF was introduced according to the required raw moments. Finally, by relaxing the density DF and total energy DF using the cascaded and BGK schemes respectively, a DDF thermal CLBM was constructed, where the density DF solves the flow field and the total energy DF solves the temperature field and they are coupled naturally by EOS for the ideal gas.

To verify the proposed model, a thermal Couette flow was simulated first, and the simulation results agreed well with the analytical solutions in different cases, which demonstrated the present TCLBM can include viscous heat dissipation with different Prandtl number and specific-heat ratio. The TCLBM's ability of simulating low-Mach compressible flows was then verified by simulating a low-Mach shock tube problem. The numerical results for the Rayleigh-Bénard and square cavity convections confirmed that the model can simulate thermal problems with force field without invoking the Boussinesq assumption.

In summary, the present TCLBM retains the simplicity and numerical efficiency of the DDF-LB method while the numerical stability of CLBM is preserved. In this method, the viscous heat dissipation and compression work are taken into account, the Prandtl number and specific-heat ratio are adjustable, and the external force is considered directly without the Boussinesq assumption. Finally, the present method can be extended to three dimensions (3D) readily based on the 3D cascaded LBM [21,25,26].

Acknowledgments

Support from the MOST National Key Research and Development Programme (Project No. 2016YFB0600805) and the Center for Combustion Energy at Tsinghua University is gratefully acknowledged.

The simulations were partly performed on the Tsinghua High-Performance Parallel Computer supported by the Tsinghua National Laboratory for Information Science and Technology and partly on ARCHER funded under the EPSRC project “UK Consortium on Mesoscale Engineering Sciences (UKCOMES)” (Grants No. EP/L00030X/1 and No. EP/R029598/1).

References

- [1] X. He, S. Chen, G.D. Doolen, A novel thermal model for the lattice Boltzmann method in incompressible limit, *J. Comput. Phys.* 146 (1) (1998) 282–300.
- [2] Z. Guo, C. Zheng, B. Shi, T. Zhao, Thermal lattice Boltzmann equation for low mach number flows: decoupling model, *Phys. Rev.* 75 (3) (2007) 036704.
- [3] J. Wang, M. Wang, Z. Li, A lattice Boltzmann algorithm for fluid–solid conjugate heat transfer, *Int. J. Therm. Sci.* 46 (3) (2007) 228–234.
- [4] Q. Li, K.H. Luo, Y. He, Y. Gao, W. Tao, Coupling lattice Boltzmann model for simulation of thermal flows on standard lattices, *Phys. Rev.* 85 (1) (2012) 016710.
- [5] H.R. Ashorynejad, A.A. Mohamad, M. Sheikholeslami, Magnetic field effects on natural convection flow of a nanofluid in a horizontal cylindrical annulus using lattice Boltzmann method, *Int. J. Therm. Sci.* 64 (2013) 240–250.
- [6] Q. Li, Q. Kang, M.M. Francois, Y. He, K.H. Luo, Lattice Boltzmann modeling of boiling heat transfer: the boiling curve and the effects of wettability, *Int. J. Heat Mass Tran.* 85 (2015) 787–796.
- [7] C. Lin, A. Xu, G. Zhang, Y. Li, Double-distribution-function discrete Boltzmann model for combustion, *Combust. Flame* 164 (2016) 137–151.
- [8] C. Lin, K.H. Luo, L. Fei, S. Succi, A multi-component discrete Boltzmann model for nonequilibrium reactive flows, *Sci. Rep.* 7 (1) (2017) 14580.
- [9] L. Fei, K.H. Luo, C. Lin, Q. Li, Modeling incompressible thermal flows using a central-moments-based lattice Boltzmann method, *Int. J. Heat Mass Tran.* 120 (2018) 624–634.
- [10] S. Succi, Lattice Boltzmann across scales: from turbulence to dna translocation, *Eur. Phys. J. B Condens. Matter Complex Syst.* 64 (3) (2008) 471–479.
- [11] Q. Li, K.H. Luo, Q. Kang, Y. He, Q. Chen, Q. Liu, Lattice Boltzmann methods for multiphase flow and phase-change heat transfer, *Prog. Energy Combust. Sci.* 52 (2016) 62–105.
- [12] Z. Guo, C. Shu, *Lattice Boltzmann Method and its Applications in Engineering* vol. 3, World Scientific, 2013.
- [13] Y. Qian, D. d’Humières, P. Lallemand, Lattice bgk models for Navier-Stokes equation, *Europhys. Lett.* 17 (6) (1992) 479.
- [14] I. Ginzburg, Equilibrium-type and link-type lattice Boltzmann models for generic advection and anisotropic-dispersion equation, *Adv. Water Resour.* 28 (11) (2005) 1171–1195.
- [15] I. Ginzburg, F. Verhaeghe, D. d’Humières, Two-relaxation-time lattice Boltzmann scheme: about parametrization, velocity, pressure and mixed boundary conditions, *Commun. Comput. Phys.* 3 (2) (2008) 427–478.
- [16] D. d’Humières, Generalized Lattice-boltzmann Equations, *Rarefied Gas Dynamics-Theory and Simulations*, (1994), pp. 450–458.
- [17] P. Lallemand, L.-S. Luo, Theory of the lattice Boltzmann method: dispersion, dissipation, isotropy, galilean invariance, Stability, *Physical Review E* 61 (6) (2000) 6546.
- [18] I. Karlin, A. Ferrante, H. Öttinger, Perfect entropy functions of the lattice Boltzmann method, *Europhys. Lett.* 47 (2) (1999) 182.
- [19] S. Ansumali, I.V. Karlin, Stabilization of the lattice Boltzmann method by the h theorem: a numerical test, *Phys. Rev.* 62 (6) (2000) 7999.
- [20] S. Ansumali, I.V. Karlin, H.C. Öttinger, Minimal entropic kinetic models for hydrodynamics, *Europhys. Lett.* 63 (6) (2003) 798.
- [21] M. Geier, A. Greiner, J.G. Korvink, Cascaded digital lattice Boltzmann automata for high Reynolds number flow, *Phys. Rev.* 73 (6) (2006) 066705.
- [22] D. Lycett-Brown, K.H. Luo, Multiphase cascaded lattice Boltzmann method, *Comput. Math. Appl.* 67 (2) (2014) 350–362.
- [23] X. Shan, H. Chen, Lattice Boltzmann model for simulating flows with multiple phases and components, *Phys. Rev.* 47 (3) (1993) 1815.
- [24] A. Kupershtokh, D. Medvedev, D. Karpov, On equations of state in a lattice Boltzmann method, *Comput. Math. Appl.* 58 (5) (2009) 965–974.
- [25] D. Lycett-Brown, K.H. Luo, R. Liu, P. Lv, Binary droplet collision simulations by a multiphase cascaded lattice Boltzmann method, *Phys. Fluids* 26 (2) (2014) 023303.
- [26] D. Lycett-Brown, K.H. Luo, Cascaded lattice Boltzmann method with improved forcing scheme for large-density-ratio multiphase flow at high Reynolds and weber numbers, *Phys. Rev.* 94 (5) (2016) 053313.
- [27] L. Fei, K.H. Luo, Consistent forcing scheme in the cascaded lattice Boltzmann method, *Phys. Rev.* 96 (5) (2017) 053307.
- [28] F.J. Alexander, S. Chen, J. Sterling, Lattice Boltzmann thermohydrodynamics, *Phys. Rev.* 47 (4) (1993) R2249.
- [29] Y. Qian, Simulating thermohydrodynamics with lattice bgk models, *J. Sci. Comput.* 8 (3) (1993) 231–242.
- [30] P. Lallemand, L.-S. Luo, Theory of the lattice Boltzmann method: acoustic and thermal properties in two and three dimensions, *Phys. Rev.* 68 (3) (2003) 036706.
- [31] P. Lallemand, L.-S. Luo, Hybrid finite-difference thermal lattice Boltzmann equation, *Int. J. Mod. Phys. B* 17 (01n02) (2003) 41–47.
- [32] I. Karlin, D. Sichau, S. Chikatamarla, Consistent two-population lattice Boltzmann model for thermal flows, *Phys. Rev.* 88 (6) (2013) 063310.
- [33] Y. Feng, P. Sagaut, W. Tao, A three dimensional lattice model for thermal compressible flow on standard lattices, *J. Comput. Phys.* 303 (2015) 514–529.
- [34] K.N. Premnath, S. Banerjee, Incorporating forcing terms in cascaded lattice Boltzmann approach by method of central moments, *Phys. Rev.* 80 (3) (2009) 036702.
- [35] N.I. Prasianakis, I.V. Karlin, Lattice Boltzmann method for thermal flow simulation on standard lattices, *Phys. Rev.* 76 (1) (2007) 016702.
- [36] H. Liepmann, A. Roshko, *Elements of Gasdynamics* John Wiley & Sons, New York.
- [37] Q. Zou, X. He, On pressure and velocity boundary conditions for the lattice Boltzmann bgk model, *Phys. Fluids* 9 (6) (1997) 1591–1598.
- [38] G. Zhao-Li, Z. Chu-Guang, S. Bao-Chang, Non-equilibrium extrapolation method for velocity and pressure boundary conditions in the lattice Boltzmann method, *Chin. Phys.* 11 (4) (2002) 366.
- [39] E.F. Toro, *Riemann Solvers and Numerical Methods for Fluid Dynamics: a Practical Introduction*, Springer Science & Business Media, 2013.
- [40] R. Clever, F. Busse, Transition to time-dependent convection, *J. Fluid Mech.* 65 (04) (1974) 625–645.
- [41] Q. Li, Y. He, Y. Wang, G. Tang, An improved thermal lattice Boltzmann model for flows without viscous heat dissipation and compression work, *Int. J. Mod. Phys. C* 19 (01) (2008) 125–150.
- [42] J. Vierendeels, B. Merci, E. Dick, Benchmark solutions for the natural convective heat transfer problem in a square cavity with large horizontal temperature differences, *Int. J. Numer. Meth. Heat Fluid Flow* 13 (8) (2003) 1057–1078.